

Switchable Charge Storage Mechanism via in Situ Activation of MXene Enables High Capacitance and Stability in Aqueous Electrolytes

Cheng-Che Hsiao,^{||} James Kasten,^{||} Denis Johnson, Bright Ngozichukwu, Ray M. S. Yoo, Seungjoo Lee, Ali Erdemir, and Abdoulaye Djire*



Cite This: *ACS Nano* 2024, 18, 7180–7191



Read Online

ACCESS |



Metrics & More



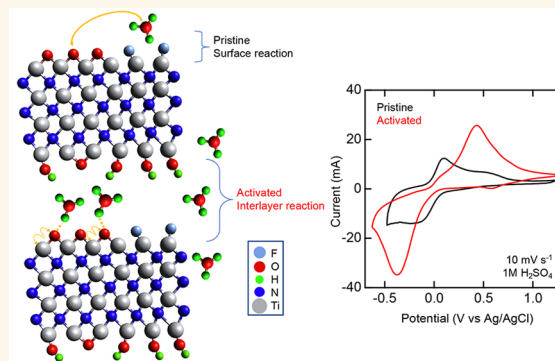
Article Recommendations



Supporting Information

ABSTRACT: The need for reliable renewable energy storage devices has become increasingly important. However, the performance of current electrochemical energy storage devices is limited by either low energy or power densities and short lifespans. Herein, we report the synthesis and characterization of multilayer $\text{Ti}_4\text{N}_3\text{T}_x$ MXene in various aqueous electrolytes. We demonstrate that $\text{Ti}_4\text{N}_3\text{T}_x$ can be electrochemically activated through continuous cation intercalation over a 10 day period using cyclic voltammetry. A wide operating window of 2 V is maintained throughout activation. After activation, capacitance at 2 mV s^{-1} increases by 300%, 140%, and 500% in 1 M H_2SO_4 , 1 M MgSO_4 , and 1 M KOH , respectively, while maintaining $\sim 600 \text{ F g}^{-1}$ at 2 mV s^{-1} after 50000 cycles in 1 M H_2SO_4 . This activation process is possibly attributed to the unique morphology of the multilayered material, allowing cation intercalation to increase access to redox-active sites between layers. This work adds to the growing repository of electrochemically stable MXenes reported for aqueous energy storage applications. These findings offer a reliable option for reliable energy storage devices with potential applications in large-scale grid storage and electric vehicles.

KEYWORDS: MXene, Energy Storage, Intercalation, Electrochemical Activation, Aqueous



1. INTRODUCTION

Improving the performance of electrochemical energy storage devices is a necessary development for efficiently harvesting energy from renewable sources and gaining independence from a fossil-fuel-based energy economy.^{1,2} Currently, batteries and supercapacitors are at the forefront of electrochemical energy storage research due to their high energy and power densities, respectively.^{3–5} On one hand, lithium-ion batteries have emerged as an industry standard for various electrical energy storage applications due to their superior energy densities.⁶ However, their low power densities and short lifespans along with the fluctuations in lithium prices and environmental concerns have pushed investigations for cheaper and more environmentally benign alternative battery systems and materials with high energy and power densities.⁷

On the other hand, electrochemical double-layer capacitors (EDLCs) are limited to only providing high power and long cycle life.

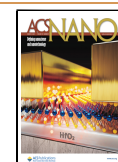
Pseudocapacitors can provide a solution to these performance gaps by combining the best attributes from EDLCs and batteries. In the search to find cost-effective and efficient materials for supercapacitors, a wide range of materials including polymers,^{8–11} chalcogenides,^{12–15} metal oxides^{16–20} and sulfides^{21–23} and high surface area transition-metal carbides^{24–27} and nitrides^{28–31} have been studied. These materials are frequently investigated due to their pseudocapacitive charge storage mechanisms involving fast and reversible Faradaic redox reactions which contribute to substantially larger capacitances compared to EDLCs.³² Current benchmark materials for supercapacitors include RuO_2 , MnO_2 , and high

Received: December 5, 2023

Revised: February 9, 2024

Accepted: February 13, 2024

Published: February 19, 2024



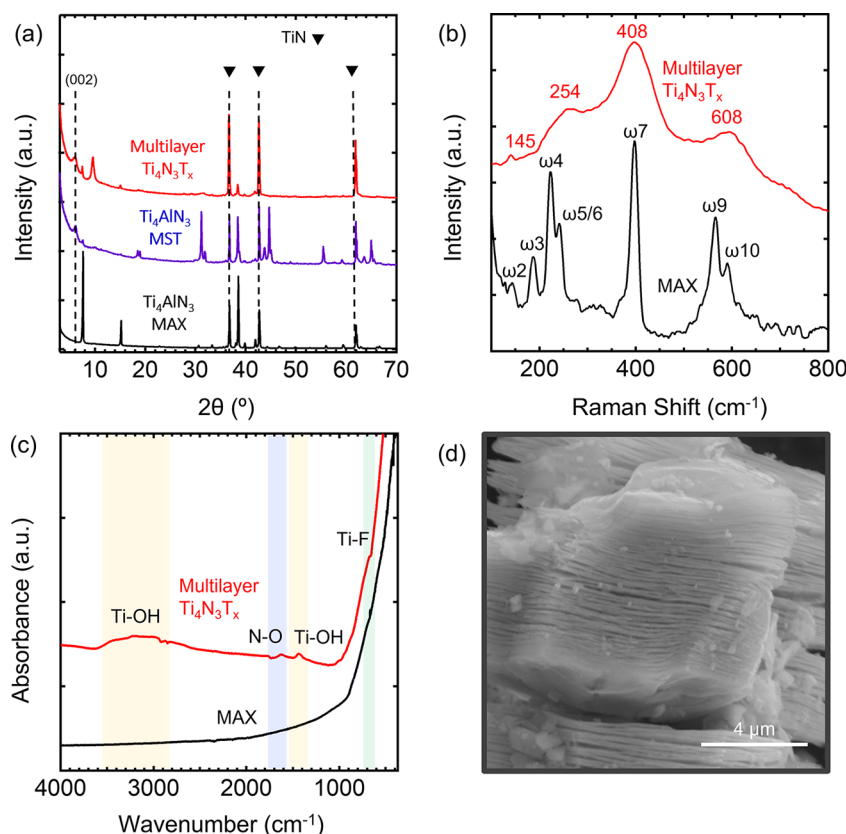


Figure 1. (a) X-ray diffraction patterns of Ti₄AlN₃ MAX phase (black), Ti₄AlN₃ molten salt fluoride treated (MST) (purple) from the O₂-assisted molten salt fluoride synthesis, and multilayer Ti₄N₃T_x MXene (red). (b) Raman and (c) FTIR spectra of MAX (black) and MXene (red). (d) SEM image for multilayer Ti₄N₃T_x MXene.

surface area VN.^{33–35} However, transition metal oxides are known for exhibiting poor electrical conductivity, requiring them to be engineered at nanoscales to achieve pseudocapacitive kinetics, and thereby limiting their application to small-scale electronics.

An emerging class of 2D transition metal carbides and nitrides known as MXenes was developed in 2011 by etching of a precursor M_{n+1}A_nX_n phase, where M represents an early d-block transition metal, A represents a group IIIA–VIA element, and X represents carbon and/or nitrogen.³⁶ The A layer can be selectively etched to produce a MXene with structure M_{n+1}X_nT_x, where T_x represents surface termination groups (–O–, –OH, –F, etc.). Currently, approximately 100 MXene compositions have been reported to theoretically exist, with most of them experimentally synthesized.³⁷ Their morphology, high conductivity, and active surface area have made them applicable materials for battery and supercapacitor research.³⁸ However, between carbide and nitride MXenes, the former has received far more attention, as there are a greater number of possible carbide compositions. Additionally, it has been reported to be significantly harder to synthesize nitride MXenes due to the high formation energy of their precursor MAX phases.³⁹ Nonetheless, nitride MXenes have been reported to possess greater conductivity, oxidative stability, and active surface area compared to their carbide counterparts.⁴⁰ Both carbide and nitride MXenes have shown great potential for aqueous supercapacitors with Ti₃C₂, V₂C, V₄C₃, and Ti₂N each obtaining high capacitances of over 200 F g⁻¹ in select aqueous electrolytes, along with V₂C and Ti₂N also obtaining stable capacitance retentions.^{41–43} However, no

MXene to date has exhibited high stability across aqueous electrolytes of different pHs, but rather selective stability in one electrolyte. Similarly, no MXene to date has been reported to possess capacitance growth in more than one aqueous environment.

In this work, we report on the electrochemical performance, in aqueous electrolytes, of multilayered Ti₄N₃T_x MXene synthesized via an oxygen-assisted molten salt etching to remove the aluminum layer of Ti₄AlN₃. MXene synthesis was verified using multiple physical characterization analyses, including X-ray diffraction (XRD), scanning electron microscopy (SEM), and Raman spectroscopy. The surface termination groups (T_x) were also characterized via Fourier transform infrared (FTIR) spectroscopy. After physical characterization, we electrochemically activated multilayered Ti₄N₃T_x through continuous cation intercalation over a 10 day period using cyclic voltammetry (CV). The electrochemical performance and capacitance of Ti₄N₃T_x were assessed before and after the activation process by using CV, electrochemical impedance spectroscopy (EIS), and galvanostatic charge–discharge (GCD) in separate 1 M aqueous solutions of H₂SO₄, MgSO₄, and KOH. Lastly, physical characterization was repeated after activation to investigate potential changes in material properties. In H₂SO₄, activation led to a switch in the charge storage mechanism from a capacitor to a capacitor–battery hybrid behavior as a result of hydronium ion intercalation, accompanied by changes in the oxidation state of Ti. Using these results, a proposed pseudocapacitive mechanism of Ti₄N₃T_x in H₂SO₄ was determined, which can

be used to warrant further understanding of nitride MXene charge storage mechanisms for energy storage applications.

2. RESULTS AND DISCUSSION

2.1. Physical Characterization of $Ti_4N_3T_x$. **2.1.1. Physical Characterization.** The XRD patterns of the Ti_4AlN_3 MAX phase precursor, molten salt treated Ti_4AlN_3 -MST, and multilayered (ML) $Ti_4N_3T_x$ MXene are shown in Figure 1a. The synthesis is corroborated by a shift in the (002) diffraction peak toward a lower angle from $2\theta = 7.56^\circ$ to 5.92° , which indicates sufficient etching of the Al layer from Ti_4AlN_3 to ML $Ti_4N_3T_x$. This shift is accompanied by an increase in the *c*-lattice parameter (*c*-LP) from 23.4 Å for the Ti_4AlN_3 MAX phase to 29.8 Å for the multilayer $Ti_4N_3T_x$, which is consistent with previously reported values.^{44–46} Furthermore, most of the peaks belonging to Ti_4AlN_3 either are absent or have significantly decreased in intensity following etching. All the peaks have been identified except that at $2\theta = 10.17^\circ$. This unknown peak seems to appear after the acid wash step, suggesting that it may be related to the interaction of the acid solution and the fluoride salts. Further studies are needed to understand the nature of this peak. Extra peaks in the Ti_4N_3 -MST spectra that are not present in the MAX phase are the expected aluminum fluoride compounds which include K_2NaAlF_6 , $K_2Li[AlF_6]$, Na_3AlF_6 , $K_2Na[AlF_4]_3$, and Na_3AlF_6 , all of which are soluble in the formic acid solution.⁴⁴ Also, additional peaks present in the multilayer MXene at $2\theta = 38.61$, 44.79 , and 65.18° are attributed to unreacted TiN which was originally present in the MAX phase.^{44,47} The physical surface area was investigated by N_2 -physisorption. The Ti_4AlN_3 MAX phase shows a surface area of $2.5\text{ m}^2\text{ g}^{-1}$ while the multilayer $Ti_4N_3T_x$ MXene displays an increase in the surface area to $18\text{ m}^2\text{ g}^{-1}$. An increase in pore diameter and pore size (Figure S1) with an increase in pore volume from about $0.007\text{ cm}^3\text{ g}^{-1}$ in the MAX to $0.05\text{ cm}^3\text{ g}^{-1}$ in the $Ti_4N_3T_x$ MXene is related to the pores generated from voids between the multilayer sheets.⁴⁴ The Raman spectrum of the Ti_4AlN_3 MAX phase (Figure 1b) is shown to be consistent with previously reported data.⁴⁸ In particular, ω_2 , ω_5 , and ω_{10} are E_{1g} group vibrations, which contain in-plane vibrational modes of Ti and N atoms.⁴⁹ After etching the Al layer, these peaks decrease and broaden due to the increased interlayer spacing of the MXene structure. Similarly, ω_4 , ω_7 , and ω_8 corresponding to A_{1g} out of plane vibrations of Ti and N atoms undergoing a red shift and broadening after the removal of the Al atom. Based on the group theory of M_4X_3 MXenes, there should be even more vibrational modes observed, as they involve more atomic layers and thus more possibilities of vibrational modes. The reason for the Ti_2NT_x and $Ti_4N_3T_x$ MXenes having the same Raman spectra is to be investigated and determined in future works. FTIR spectroscopy was used to identify the surface termination groups of the synthesized multilayer $Ti_4N_3T_x$ MXene (Figure 1c). The broad and predominant peaks that emerge at 3300 and 1400 cm^{-1} are assigned to the vibrational stretching and bending of the OH group. The peak at 1600 cm^{-1} indicates N–H bonding resulting from the sublattice N atoms being exposed during acid washing.⁵⁰ SEM was employed to investigate the morphology, completion of the etching process, and structural defects of both the Ti_4AlN_3 MAX (Figure S2a) and the multilayer $Ti_4N_3T_x$ MXene (Figure 1d). The morphology of the MAX shows that the titanium nitride layers are held firmly together by the aluminum. However, the SEM of the MXene

reveals a large interlayer distance between each flake, confirming etching of the Al layers from the parent MAX.⁵¹ Compositional analysis of the MAX and the MXene was performed using energy-dispersive X-ray spectroscopy (EDS) to gain insight into the atomic ratio of the Ti, Al, and N elements. Results confirm the removal of the Al with a negligible amount left compared to the MAX. The various atomic ratios are given in Figure S2. Residual K still present in the MXene arises from the molten salt fluoride used during the etching process.

2.1.2. X-ray Absorption Spectroscopy. X-ray absorption spectroscopy (XAS) was performed to gather insight into how material oxidation state shifts during synthesis. Through analysis of the X-ray absorption near edge structure (XANES) region (Figure 2a), it can be observed that the

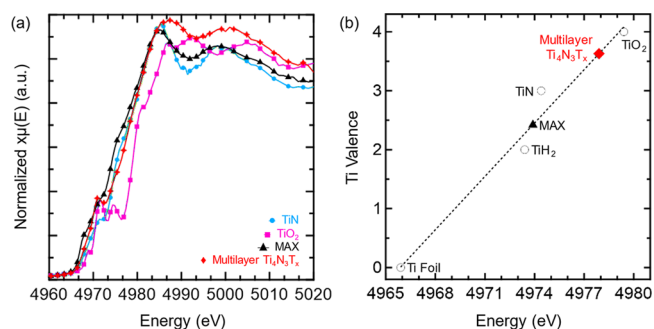


Figure 2. (a) XANES region of the normalized Ti K-edge XAS spectra for TiN (blue), TiO₂ (magenta), Ti₄AlN₃ MAX (black), and multilayer Ti₄N₃T_x (red) materials. TiN and TiO₂ are used as calibration standards. (b) Edge position determined from XANES spectra of several Ti reference compounds (hollow circles), Ti₄AlN₃ MAX (black triangle), and multilayer Ti₄N₃T_x (red diamond) as a function of Ti valency.

MAX phase (black trace) lies to the left of the TiN (blue) reference curve. Upon etching, the Ti K-edge peaks of MXene (red) shift to the right to lie between the TiN and TiO₂ (purple) reference samples. This is further corroboration of the etching of the Al layers and integration of oxygen surface termination groups.^{52,53} The XANES data were further investigated to ascertain the valency of the Ti atoms in the MAX and MXene structures. Based on the calibration curve generated by taking the derivative of the reference curves and finding peak energy values (Figure 2b), a calibration curve can be generated with an R^2 value of 0.97, indicating high reliability of the curve. The calculated reference values are also in line with values from the literature, indicating high accuracy for further analysis.^{54,55} From this calibration curve, the Ti₄AlN₃ MAX phase has a Ti valency of 2.4, while the multilayer Ti₄N₃T_x MXene has a Ti valency of 3.6. The deviation from the expected +3 valency can be attributed to the other bonds being made by the Ti atoms in the structure. Lower Ti oxidation states in the MAX are attributed to metal–metal Ti–Al bonds to form the 3D cross-links. Meanwhile, in the MXene structure, Ti atoms simultaneously participate in a combination of +3 Ti–N bonds and multiple +2 bonds with termination groups to a single Ti atom.

2.2. Electrochemical Results. The intercalation of cations, such as Li⁺, Na⁺, Mg²⁺, and K⁺, has been demonstrated for carbide MXenes, but no interaction chemistry has been extensively reported for nitride MXenes. For Ti₃C₂T_x, this intercalation has led to high pseudocapacitance with adequate

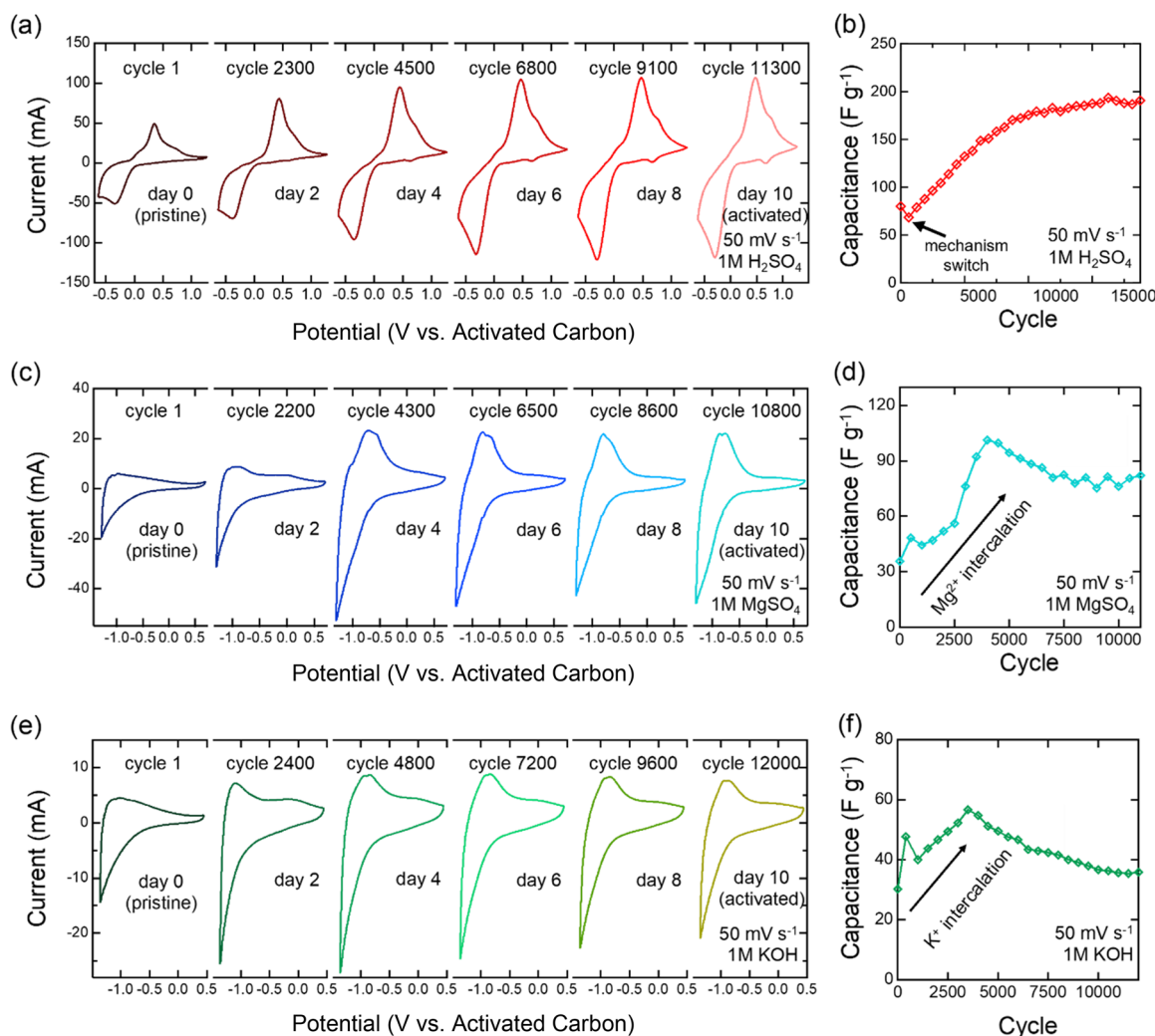


Figure 3. CV and specific capacitance evolution of multilayered $\text{Ti}_4\text{N}_3\text{T}_x$ electrode subjected to continuous cycling over a 10 day period in (a, b) 1 M H_2SO_4 , (c, d) 1 M MgSO_4 , and (e, f) 1 M KOH. CV measurements were taken at a 50 mV s^{-1} scan rate.

stability, especially in aqueous electrolytes.⁴¹ Here, we use this intercalation chemistry to activate nitride MXene electrodes in acidic, basic, and neutral aqueous electrolytes over wide voltage windows and to increase capacitance over time. We use 1 M solutions of H_2SO_4 , MgSO_4 , and KOH to represent the different pH regimes—acid, neutral, and base. To activate the material, we cycled a fresh electrode in each of the electrolytes using CV at a scan rate of 50 mV s^{-1} . The activation consists of intercalating H_3O^+ , Mg^{2+} , and K^+ into the layers of $\text{Ti}_4\text{N}_3\text{T}_x$ ($\text{T}_x = \text{O}, \text{OH},$ and F) and oxidizing and reducing the inner layer Ti, which are otherwise not accessible during conventional charge storage. To achieve full activation, the CV cycling was continued for 10 days in each electrolyte. After full activation, the capacitance is expected to increase.

2.2.1. Electrochemical Intercalation and Capacitance Evolution. After material synthesis and electrode preparation, electrochemical measurements were conducted in aqueous 1 M H_2SO_4 , MgSO_4 , and KOH electrolytes. Each electrode was tested in a fresh electrolyte and was electrochemically activated. Cyclic voltammetry (CV) scans reveal a wide voltage window of 1.9 V in 1 M H_2SO_4 (Figure 3a) electrolyte. As shown in Figure 3b, capacitance increases from $\sim 70 \text{ F g}^{-1}$ to $\sim 190 \text{ F g}^{-1}$ at a 50 mV s^{-1} scan rate, representing a capacitance retention of 270% over the 10 day period of

continuous cycling. The redox peaks seen in Figure 3a may be attributed to a quasi-reversible protonation between aqueous hydronium and $-\text{O}-$ surface termination groups present between MXene layers, which is discussed later. The growth in these peaks during cycling indicates improved Faradaic charge-storage behavior between layers, which is consistent with the capacitance results in Figure 3b.

In alkaline and neutral systems, $\text{Ti}_4\text{N}_3\text{T}_x$ MXene exhibits working voltage windows of 2.0 V in MgSO_4 (Figure 3c) and 1.8 V in KOH (Figure 3e). Pseudocapacitive activity can be observed in the cathodic region of both neutral and basic electrolytes due to the intercalation of cations (K^+ , Mg^{2+}).⁴¹ Moreover, the CV shape in MgSO_4 appears similar to that in previous nitride MXene works, demonstrating pseudocapacitive behavior.⁵⁶ It is worth noting that hydrogen evolution becomes more pronounced during activation. Moreover, the capacitance reached its maximum between cycle 3000 and 5000 (Figure 3d), with over 100 F g^{-1} in MgSO_4 and about 60 F g^{-1} in KOH electrolyte at 50 mV s^{-1} . After reaching the maximum, the capacitance then stabilizes. In MgSO_4 and KOH, the capacitance retentions are about 220% and 125%, respectively, at the end of the 10 day activation period.

2.2.2. Capacitance Comparison between Pristine and Activated Electrodes. After the working voltage window was

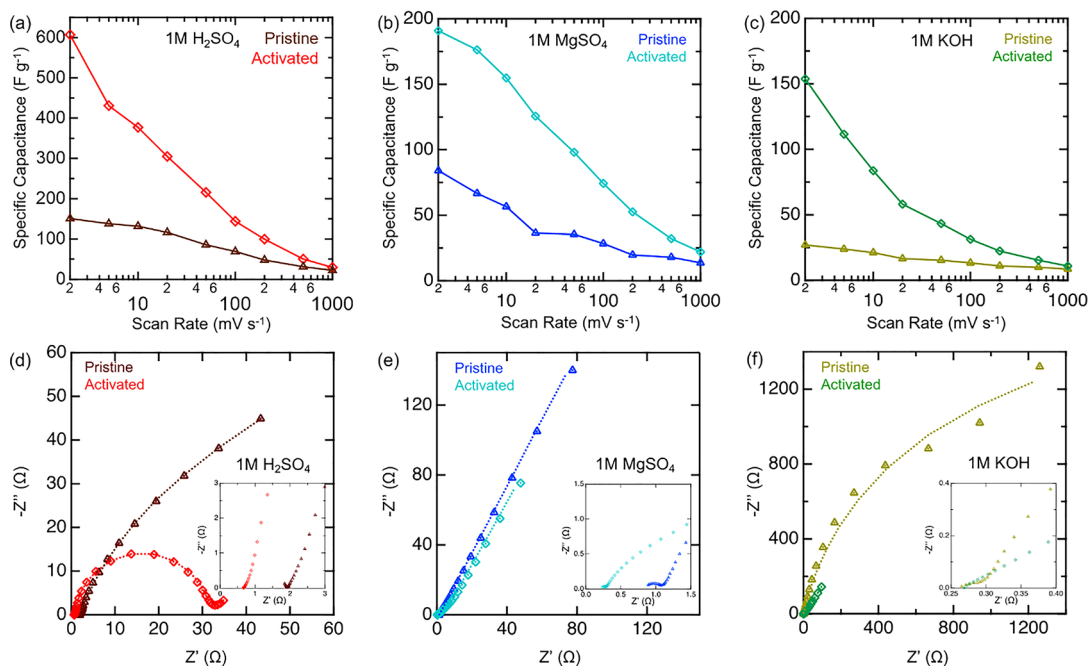


Figure 4. Comparison of electrochemical behavior of pristine (triangle) and activated (diamond) multilayered $\text{Ti}_4\text{N}_3\text{T}_x$ electrodes in (a, d) 1 M H_2SO_4 , (b, e) 1 M MgSO_4 , and (c, f) 1 M KOH electrolyte. (a–c) Specific capacitance of $\text{Ti}_4\text{N}_3\text{T}_x$ as a function of scan rate. (d–f) Nyquist plots of the $\text{Ti}_4\text{N}_3\text{T}_x$ electrodes including the circuit fitting.

determined, CV at scan rates from 2 to 1000 mV s^{-1} were taken for pristine and activated $\text{Ti}_4\text{N}_3\text{T}_x$. The gravimetric capacitances were then calculated for H_2SO_4 , MgSO_4 , and KOH based on the active material mass loading (Figure 4a–c). Activated electrodes exhibited capacitances of over 600 F g^{-1} in H_2SO_4 , 190 F g^{-1} in MgSO_4 , and 150 F g^{-1} in KOH electrolyte. Moreover, the capacitance values at 2 mV s^{-1} increased after activation by 300% in H_2SO_4 , 140% in MgSO_4 , and 500% in KOH. The increase in capacitance of the electrodes is likely due to the intercalation of cations between the MXene layers. Further analysis of the activation mechanism will be investigated in future works.

2.2.3. Electrochemical Impedance Spectroscopy. Electrochemical impedance spectroscopy (EIS) was used before and after activation in each electrolyte to gain insight on the processes occurring at the electrode–electrolyte interface. All Nyquist plots were collected centered at open circuit potential (OCP). Prior to activation, the EIS spectrum in H_2SO_4 (Figure 4d) revealed a very fast surface-controlled double-layer process followed by an ion diffusion process, as evidenced by an inconspicuous semicircle followed by an inclined line in the spectrum. However, after activation in H_2SO_4 , the electrode's spectrum switches to a large semicircle, characteristic of a much slower charge transfer step followed by an inclined line for the ion diffusion process. This “switch” in the charge storage mechanism is likely the result of the hydronium ions successively intercalating between the layers of the multilayered $\text{Ti}_4\text{N}_3\text{T}_x$ followed by protonation and deprotonation of $-\text{O}-$ termination groups. This redox process is evidenced by the redox couple in the CV. However, this “switch” phenomenon was not observed in the EIS spectra of MgSO_4 (Figure 4e) and KOH (Figure 4f) electrolytes, which is also consistent with the CV results, where a rapid non-Faradaic process in the high-frequency region followed by an ion diffusion process in the low-frequency region was observed in each. The EIS spectra show consistent capacitive behavior for

both pristine and activated material. Interestingly, the equivalent series resistance (ESR) in H_2SO_4 and MgSO_4 systems was reduced via the activation process but remained about the same in KOH.

2.2.4. Galvanostatic Charge–Discharge. Galvanostatic charge–discharge (GCD) curves were taken at varying charge/discharge rates from 2 to 100 A g^{-1} to further investigate the charge storage mechanism and the energy storage performance before and after activation. Following activation, the charge/discharge times increased in each electrolyte, indicating a higher capacity. Like EIS, GCD results suggest a “switch” in the charge storage mechanism in the H_2SO_4 activated $\text{Ti}_4\text{N}_3\text{T}_x$. The discharge curve after activation in H_2SO_4 displays a mixed capacitive and battery behavior, as evidenced by a sharp voltage drop followed by a plateau (Figure 5a). The sharp drop indicates the rapid double-layer capacitive discharge, while the plateau represents the slower diffusion of ions between the layers of the multilayered $\text{Ti}_4\text{N}_3\text{T}_x$. Meanwhile, only pseudocapacitive behavior was observed in the discharge curves for the MgSO_4 and KOH electrolytes (Figure 5b,c). After activation, capacities of 50, 65, and 17 mAh g^{-1} were exhibited in H_2SO_4 , MgSO_4 , and KOH electrolytes, respectively. This corresponds to increases of 100% in H_2SO_4 , 400% in MgSO_4 , and 600% in KOH at 2 A g^{-1} (Figures S5–S7).

2.2.5. Charge Storage Kinetics. The charge storage kinetics were studied by analyzing the scan rate dependence of the peak current (Figure 6), using the equation⁵⁷

$$i_p = av^b \quad (1)$$

where i_p is the gravimetric current in A g^{-1} , v is the scan rate in mV s^{-1} , and a and b are fitting parameters. The b value is utilized to obtain insights into the charge storage kinetics. For example, a b value of 1 represents capacitive storage with fast diffusion, whereas a value of 0.5 indicates diffusion-controlled

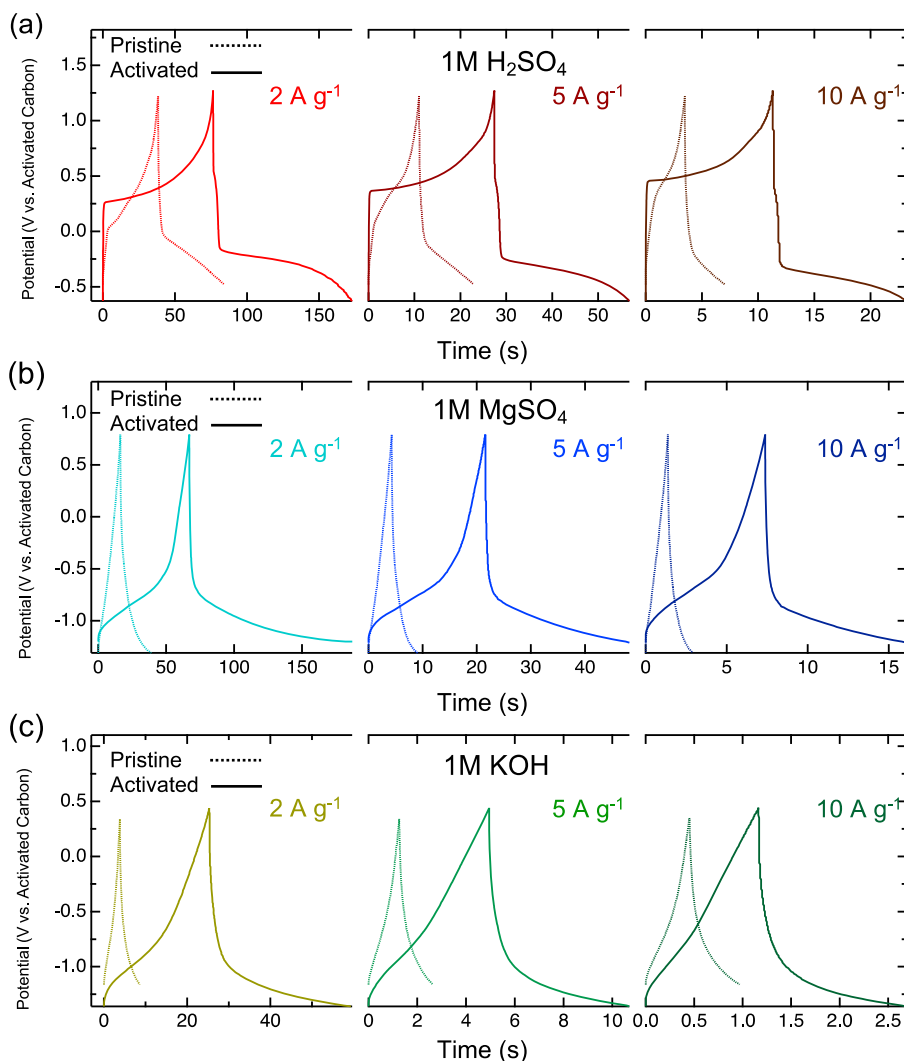


Figure 5. Galvanostatic charge–discharge curves of multilayered $\text{Ti}_4\text{N}_3\text{T}_x$ electrodes at different current densities in (a) 1 M H_2SO_4 , (b) 1 M MgSO_4 and (c) 1 M KOH . The dashed and solid lines represent the pristine and activated electrode, respectively. The charge–discharge curves are consistent with the different current densities.

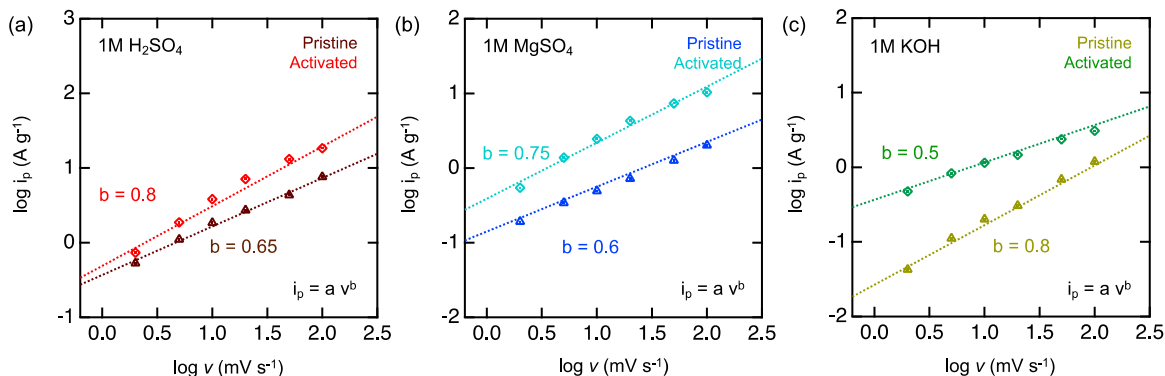


Figure 6. Scan rate dependence of the current for multilayered $\text{Ti}_4\text{N}_3\text{T}_x$ in (a) H_2SO_4 (brown, red), (b) MgSO_4 (navy, light blue), and (c) KOH (mustard, green) electrolytes before (triangles) and after (diamonds) the activation. The dashed line is the linear fit of each data set.

processes. In H_2SO_4 (Figure 6a), during activation, the b value increases from 0.65 to 0.8, indicating charge storage is less limited by diffusion after activation. These kinetics are representative of previous reports studying pure MXene electrodes for aqueous supercapacitors.⁴² This phenomenon may be attributed to hydronium ions already being intercalated

between the layers of MXene. In neutral electrolyte (Figure 6b), a similar phenomenon occurs wherein capacitive behavior and diffusion-controlled processes contribute to the kinetics of the activated electrode. In alkaline electrolyte (Figure 6c), however, the b value decreases from 0.8 to 0.5, indicating the kinetics is limited by ion diffusion. This is further reflected by

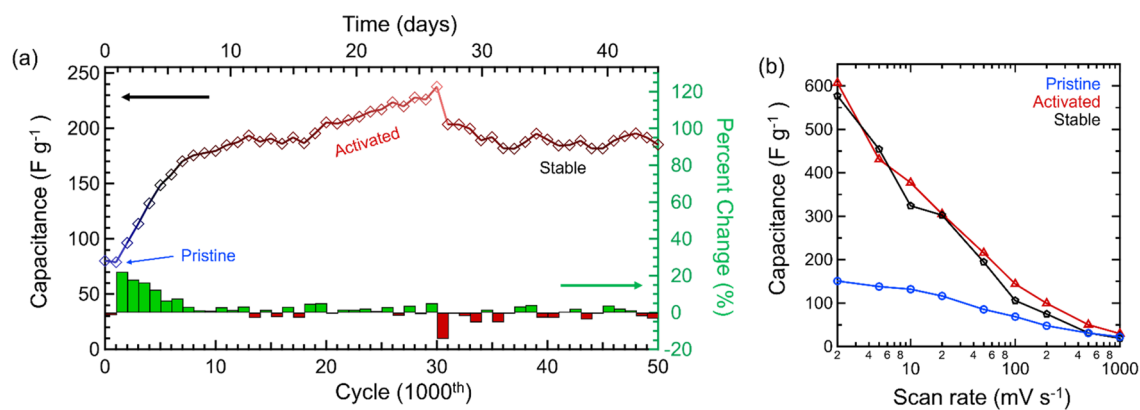


Figure 7. CV stability of multilayered $\text{Ti}_4\text{N}_3\text{T}_x$ in 1 M H_2SO_4 at 50 mV s^{-1} over 50000 cycles (44 days). (a) Specific capacitance and percent change across CV cycling. (b) Specific capacitance as a function of scan rate at pristine (blue), activated (red), and stable (black) regions.

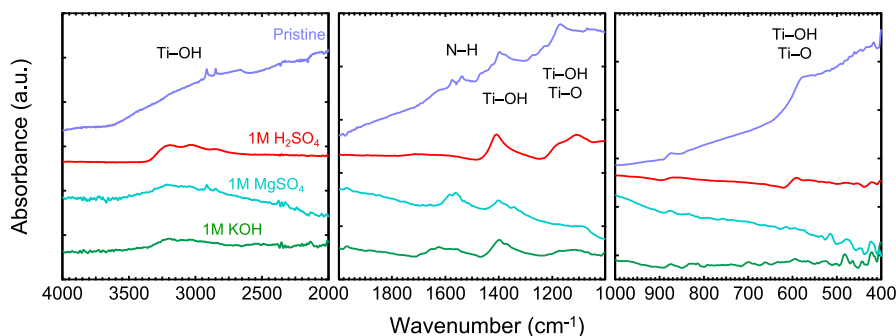


Figure 8. FTIR spectra of the multilayered $\text{Ti}_4\text{N}_3\text{T}_x$ MXene electrodes before (dark blue) and after activation in 1 M H_2SO_4 (red), MgSO_4 (light blue), and KOH (green).

the steady decrease in capacitance following activation before stabilization and may be attributed to the solution pH. Further studies involving more invasive techniques, such as in situ XRD and EQCM, being conducted during activation will reveal more about the electrolyte effect on kinetics over time.

2.2.6. Long-Term Stability. To evaluate long-term performance, in addition to activation, CV was continuously run in 1 M H_2SO_4 totalling 50000 cycles over the course of 44 days (Figure 7a). Following activation, capacitance stabilizes at $\sim 190 \text{ F g}^{-1}$ for 5000 cycles before gradually increasing to a maximum capacitance of 237 F g^{-1} at 30000 cycles. After 30000 cycles capacitance consistently restabilizes to $190 \pm 5 \text{ F g}^{-1}$ for the remaining 20000 cycles. Although performance appears to decrease after 30000 cycles, capacitance across scan rate is maintained from cycle 15000 to cycle 50000 (Figure 7b), reaching over 575 F g^{-1} at 2 mV s^{-1} . There have been many reports on as-synthesized MXenes evaluated as aqueous supercapacitor electrodes, but very few exhibit long-term capacitance retentions $>100\%$ and across multiple systems as shown in this report (Table S1).^{41,42,56,58–61} Recently, shear delamination has been effective at producing Ti_3C_2 sheets with cycle lives of up to 500000 CV cycles at a capacitance retention of $\sim 96\%$.⁶² However, to date, no other work has observed an increase and stabilization of as-synthesized multilayered MXene for the time scale observed in this work.

2.3. Post Characterization. **2.3.1. Fourier Transform Infrared Spectroscopy.** To understand the effect of activation on the surface termination groups of MXene, FTIR spectroscopy was performed before and after activation in H_2SO_4 , MgSO_4 , and KOH electrolytes (Figure 8). For all pristine and activated samples, the FTIR analysis revealed the presence of

characteristic peaks at ~ 3300 and $\sim 1400 \text{ cm}^{-1}$, which are assigned to the stretching and bending vibrations of the $-\text{OH}$ group, arising from the strong adsorption and coordination of water molecules on the electrode surface. It is well-known that the hydroxyl groups can act as active sites for electrochemical reactions, ultimately leading to an improvement in energy storage.⁶³ A peak at $\sim 1550 \text{ cm}^{-1}$, arising from the vibrational N–H stretching bonds, is present in both the KOH and MgSO_4 electrodes, while being absent in the H_2SO_4 sample. A plausible explanation for the absence of this peak in the H_2SO_4 sample could be the presence of excess protons in the electrolyte allowing for the reduction of the N–H bond. In addition, a broad peak centered between 500 and 600 cm^{-1} was detected in the pristine and activated electrode in H_2SO_4 electrolyte but was absent in both KOH and MgSO_4 . These peaks are indicative of Ti–O and Ti–OH surface groups, respectively. Furthermore, the predominantly broad vibrational peak of Ti–O and Ti–OH groups at $\sim 1100 \text{ cm}^{-1}$ was observed in all electrodes.⁶⁴

2.3.2. Raman Spectroscopy. To analyze and visualize the structural changes arising from the electrochemical processes, Raman mapping of the activated $\text{Ti}_4\text{N}_3\text{T}_x$ electrodes was conducted. Due to the greatest change in potential mechanism, analysis of the H_2SO_4 -activated $\text{Ti}_4\text{N}_3\text{T}_x$ was conducted first (Figure 9a,b). The mapped spectrum displays the pristine (blue) and modified (red) areas of the material, based on the two Raman spectra observed in this region (Figure 9g, blue and red traces, respectively). Specifically, with the material activated under the H_2SO_4 electrolyte, we see a splitting of the A_{1g} vibrational mode at 610 cm^{-1} , which has not been previously reported. This split can potentially be attributed to

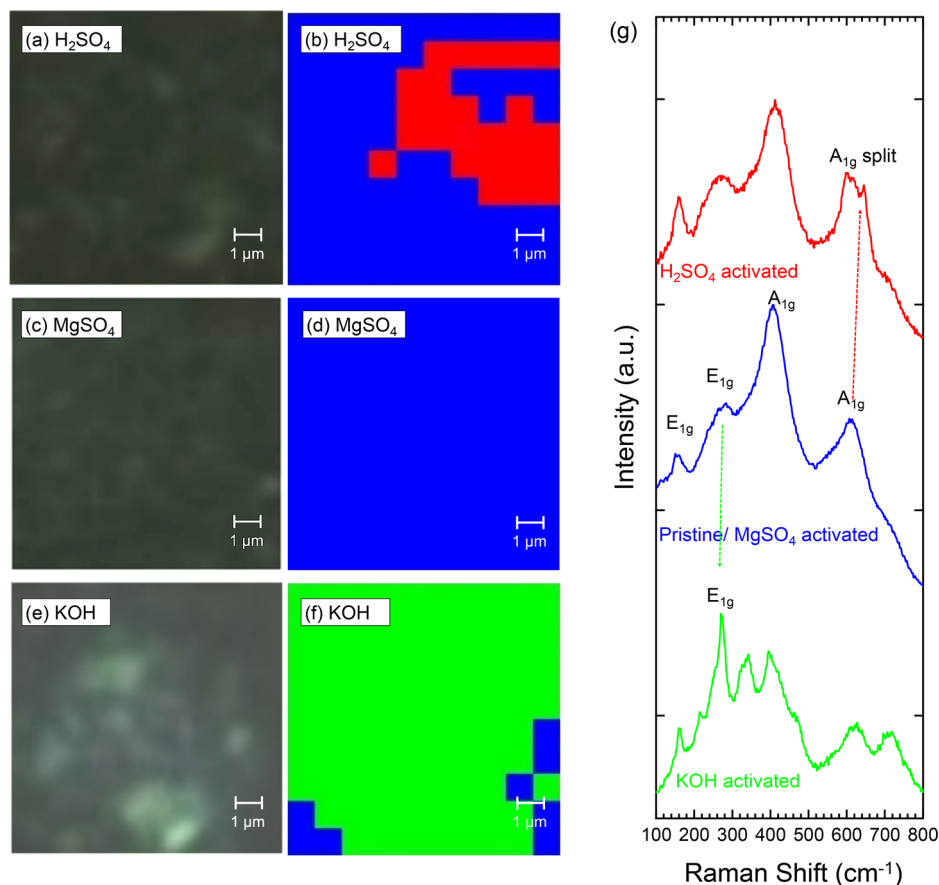
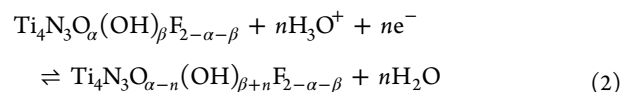


Figure 9. Raman mapping and the corresponding white light image of activated $\text{Ti}_4\text{N}_3\text{T}_x$ MXene after electrochemical characterization in (a, b) H_2SO_4 , (c, d) MgSO_4 , and (e, f) KOH . The blue spots indicate that the gathered spectrum is consistent with the pristine electrode. The red spots indicate the presence of splitting of the A_{1g} vibrational mode in the $\text{Ti}_4\text{N}_3\text{T}_x$ MXene spectrum. The green spots indicate where modification of the E_{1g} vibrational mode at 426 cm^{-1} occurs. (g) Raman spectra of pristine and activated $\text{Ti}_4\text{N}_3\text{T}_x$ MXene. All spectra were collected using a 532 nm laser, with 100% laser power, 10 s exposure time, 1800 lines/mm grating, and 100 \times objective lens.

the change in symmetry at the boundary layer and due to the electronic effects of the intercalant species, based on similar phenomena observed in graphite systems.^{65–67} Furthermore, it seems likely that the change in observed vibrational modes comes from the reorganization of the multilayered $\text{Ti}_4\text{N}_3\text{T}_x$ MXene structure rather than from intercalated ions. Specifically, due to the multilayered structure of the material, during charge storage under H_2SO_4 , the out of plane A_{1g} vibrational modes of Ti and N atoms are split into modes adjacent and nonadjacent to the intercalate layer species planes. We hypothesize that this is due to an intercalated layer being created during activation in H_2SO_4 . Furthermore, due to this information, the mapped spectrum plot (Figure 9b) is able to provide details on the quantity of the MXene surface that has encountered structural modification via ion intercalation. Approximately 25% of the electrode material is observed to have undergone structural reconfiguration for the charge storage mechanism. It seems most likely that H^+ , and not SO_4^{2-} , is intercalated into the $\text{Ti}_4\text{N}_3\text{T}_x$ MXene, as we note that with electrochemical activation under MgSO_4 electrolyte (Figure 9c,d,g, blue trace), the Raman spectrum of the activated material remains unchanged. Additionally, due to the negative surface charge typically on MXenes, cations are usually the only ions to intercalate between the layers. Further analysis of the MgSO_4 -activated $\text{Ti}_4\text{N}_3\text{T}_x$ material shows that no significant structural changes occurred during the electro-

chemical experiments. Finally, for the KOH -activated $\text{Ti}_4\text{N}_3\text{T}_x$ (Figure 9e–g, green trace), splitting of the E_{1g} vibrational mode of Ti and N atoms at 254 cm^{-1} and A_{1g} vibrational mode at 426 cm^{-1} are observed, which is in accordance with similar cation intercalation as mentioned above. It is notable that the adjusted spectra show indication of high degrees of intercalation due to the increase in structural modification from the modified E_{1g} and A_{1g} bands. Compared to 25% of the material being modified in the H_2SO_4 system, 90% of the mapped spots of the electrode material (Figure 9e,f) are shown to be involved in intercalation, thereby highlighting the compatibility of the KOH electrolyte as observed with the 125% capacitance retention.

2.4. Proposed Charge Storage Mechanism. XAS data obtained corroborate that multiple titanium oxidation states (Ti^{2+} , Ti^{3+} , and Ti^{4+}) coexist in $\text{Ti}_4\text{N}_3\text{T}_x$ MXene, with a higher proportion of Ti^{4+} in MXene compared to MAX.⁶⁸ In H_2SO_4 electrolyte, the hydronium ions likely assist the redox reactions, resulting in the titanium oxidation state change. Since the termination groups consist of $-\text{OH}$, $-\text{O}-$, and $-\text{F}$, the following pseudocapacitive redox reaction is proposed:



This mechanism involves the $-O-$ termination groups being protonated by solvated hydronium ions, which results in the formation of $-OH$ termination groups and vacant Ti sites. The vacant Ti sites are active and would undergo redox reactions in the acidic environment. Due to the multilayered structure of $Ti_4N_3T_x$, the active Ti sites between the layers are accessible by electrolyte ions, leading to interlayer storage and increased capacitance as evidenced by the emergence of a broad, separated redox couple on the CV obtained from the acidic electrolyte.

3. CONCLUSION

We reported the synthesis of multilayered $Ti_4N_3T_x$ MXene by etching the precursor Ti_4AlN_3 MAX phase using an oxygen-assisted molten salt fluoride treatment. XRD and SEM analyses indicate etching by a characteristic downshift in the (002) peak and an emergence of multilayered accordion-like morphology in the material, respectively. FTIR spectra suggest a mixture of $-F$, $-O-$, and $-OH$ surface termination groups apparent on the MXene. The electrochemical performance of the multilayered $Ti_4N_3T_x$ MXene was characterized in 1 M aqueous H_2SO_4 , $MgSO_4$, and KOH electrolytes. In each electrolyte, electrochemical activation of the material occurred when performing cyclic voltammetry at a 50 mV s^{-1} scan rate over a 10 day period (up to 12000 cycles), leading to capacitance at 2 mV s^{-1} increasing by 300% in H_2SO_4 , 140% in $MgSO_4$, and 500% in KOH. Overall, the capacitance was highest in H_2SO_4 before and after activation, achieving 125 F g^{-1} and over 575 F g^{-1} , respectively. The capacitance increase in H_2SO_4 has been attributed to an interlayer redox charge storage mechanism occurring between the acidic protons and the $-O-$ termination groups. The capacitance increase in $MgSO_4$ and KOH has been attributed to a successive ion intercalation pseudocapacitive mechanism from the Mg^{2+} and K^+ ions, respectively. Moreover, following activation in H_2SO_4 , changes to the material's EIS spectra and GCD curves further indicate the presence of Faradaic redox reactions as the dominant charge storage mechanism. Physical characterization of the $Ti_4N_3T_x$ MXene before and after electrochemical characterization also showed maintained structural and morphological integrity of the material in each electrolyte, with some surface oxidation occurring after activation. We believe that the activation period can be reduced through further studies which are currently underway. Moreover, the large operating voltage window of multilayered $Ti_4N_3T_x$ in aqueous environments warrants investigation into the performance of the material in nonaqueous systems and in two-electrode devices where larger operating windows may be achieved.

4. EXPERIMENTAL SECTION/METHODS

4.1. Material Synthesis. *4.1.1. Synthesis of Ti_4AlN_3 MAX.* The Ti_4AlN_3 MAX phase was synthesized by grinding powders of Ti (Sigma-Aldrich, 99.7%, 100 mesh), Al (Sigma-Aldrich, 99%, 30 μm), and TiN (Sigma-Aldrich, 99%, 3 μm) in a 1:1.2:2.05 molar ratio in an agate mortar for 10 min. The mix was then sintered in a tube furnace (CM Furnace Inc. 1730-20 HT) at $1400\text{ }^\circ\text{C}$ for 30 h at a ramp rate of $10\text{ }^\circ\text{C min}^{-1}$ under a constant Ar flow (Airgas, Ultra High Purity). The resulting Ti_4AlN_3 pellet was ground in an agate mortar in preparation for etching.

4.1.2. Synthesis of Molten Salt Treated Ti_4AlN_3 (Ti_4AlN_3 -MST). The $Ti_4N_3T_x$ MXene was synthesized via selective etching of the Al layer from the Ti_4AlN_3 MAX phase powder using an oxygen-assisted molten salt treatment method. The molten salt fluoride (MSF) mixture consisted of KF (Alfa Aesar, 99%), LiF (Alfa Aesar, 325 mesh,

98.5%), and NaF (Alfa Aesar, 99%), in a eutectic mass ratio of 59:29:12 and was mixed with the already synthesized Ti_4AlN_3 MAX powder in a 1:1 mass ratio. The combined MAX:MSF mixture was then ground for about 10 min in an agate mortar and transferred into a crucible boat, which was placed in a quartz tube furnace (ATS Series 3210). The furnace was ramped at a rate of $10\text{ }^\circ\text{C min}^{-1}$ up to $550\text{ }^\circ\text{C}$ and held for 5 h under a constant Ar flow of 360 mL min^{-1} . Afterward, the Ar flow was shut off, and the other end of the tube with outlet 3/16 in. ID tubing was opened to air for 1 h to allow for controlled oxygen flow. The furnace was then sealed for 2 h for continued etching of the Al from the MAX:MSF mixture. After this time, the tube furnace was turned off and allowed to cool to room temperature. The Ti_4AlN_3 -MST was then collected, weighed, and transferred into a vial.

4.1.3. Synthesis of Multilayer (ML) $Ti_4N_3T_x$ MXene. About 0.5 g of the etched Ti_4AlN_3 -MST was ground and acid-washed by mixing with 20 mL of 4 M formic acid (Sigma-Aldrich, 95%) in a beaker similar to previous synthesis work with Ti_2NT_x .^{50,69} The beaker contents were stirred for 1 h at 500 rpm using a Teflon-lined stir bar. The resulting solution was then membrane-filtered onto a 0.10 μm polycarbonate membrane (Whatman Nucleopore) and washed continuously by adding deionized water ($18.2\text{ M}\Omega\text{ cm}$, Milli-Q) until a pH of 6 was attained. At the end of the wash cycle, the $Ti_4N_3T_x$ was then collected, dried in a vacuum oven at $40\text{ }^\circ\text{C}$ overnight, transferred into a vial, and stored in a glovebox.

4.2. Physical Characterization. The bulk crystalline structure of the material was characterized by X-ray diffraction (XRD) using a Rigaku Miniflex 6G X-ray diffractometer equipped with Cu $K\alpha$ radiation ($\lambda = 0.154\text{ nm}$). The XRD was operated over a 2θ range of 3° to 70° at a scan rate of $2.0^\circ\text{ min}^{-1}$. FTIR was conducted on a Bruker INVENIO-R instrument with a diamond ATR module installed. Physical surface area was determined by N_2 -physisorption (Quantachrome Autosorb-iQ) with the Brunauer–Emmett–Teller (BET) method. The material was degassed in vacuum at $80\text{ }^\circ\text{C}$ for 6 h before the measurement. Raman spectroscopy was carried out using a Renishaw inVia Qontor instrument with a 532 nm laser, an 1800 lines/mm grating, and a 50 \times long objective lens, unless stated otherwise. The morphology of the MXenes was observed with a JSM-IT200 scanning electron microscope (SEM) equipped with energy-dispersive X-ray spectroscopy (EDS). Surface characterizations were performed using X-ray photoelectron spectroscopy (XPS), Omicron XPS system with Argus detector courtesy of TAMU Materials Characterization Facility, RRID:SCR_022202). For survey scans, XPS analysis was done with the CAE as 100 eV and the dwell time as 0.05 s. For high-resolution scans, XPS analysis was done with the CAE as 40 eV and the dwell time as 0.05 s, with three spectra collected to be averaged out for the overall scan. For the X-ray 558 Control, the emission current was set to 15 mA and the anode current to 15 kV, making the X-ray power 225. For the CN10 neutralizer settings, the emission current was set at 10 MA and the beam energy at 2 eV. The aperture was set at 3 or 5, making the aperture coefficients a and b 304.3 and 0.91 or 39.2 and 0.43, respectively. XAS measurements were performed in fluorescence mode at the multipurpose beamline for spectroscopy, 12-BM, at the Advanced Photon Source (APS) located at Argonne National Laboratory (ANL). A defined beam size of $0.5 \times 0.8\text{ mm}^2$ using slits and an incident photon flux of $\sim 10^{11}$ photons s^{-1} were used. XANES data were collected in the vicinity of the Ti K-edge (4966 eV) at ambient temperature. Ti foil, TiH₂, TiN, and TiO₂ rutile were investigated in fluorescence to obtain the reference spectra. XAS data were processed using the Demeter software package with the built-in AUTOBK algorithm used to normalize the absorption coefficient.

4.3. Electrode Preparation. Electrodes were prepared via a slurry method with the composition of 85% $Ti_4N_3T_x$ MXene, 10% carbon black (Super P, Alfa Aesar) and 5% polyvinylidene fluoride (PVDF) in *N*-methyl-2-pyrrolidone (NMP). Additional NMP was added to the mixture, until a preferred slurry consistency was achieved. The slurries were then manually painted onto 18 mm diameter conductive carbon paper substrates ($5.8\text{ m}\Omega\text{ cm}^{-1}$, MSE Supplies) and dried in a vacuum oven for 8 h at $80\text{ }^\circ\text{C}$. Electrode mass was obtained by

subtracting the substrate mass from the total mass after drying. A mass loading of ~3 mg was used for each electrode.

4.4. Electrochemical Cell Setup. The experiment was carried out in a three-electrode setup (PAT Series, EL-Cell) with a $\text{Ti}_4\text{N}_3\text{T}_x$ MXene electrode as the working electrode, activated carbon on stainless steel as a pseudoreference electrode, and a conductive carbon cloth as a counter electrode ($1000 \text{ m}^2 \text{ g}^{-1}$, MSE Supplies). Activated carbon was used as a pseudoreference electrode to simulate performance in an asymmetric two-electrode setup. Titanium foil acted as a single-use current collector for both the working and counter electrodes. Working and counter electrodes were separated using two porous separators ($21.6 \text{ mm} \times 0.26 \text{ mm}$) saturated with approximately $250 \mu\text{L}$ of electrolyte.

4.5. Electrochemical Measurements. All electrochemical measurements were performed using a Biologic SP-300 potentiostat. The electrodes were tested in aqueous $1 \text{ M H}_2\text{SO}_4$, 1 M MgSO_4 , and 1 M KOH solutions. Galvanostatic charge–discharge (GCD) and potentiostatic electrochemical impedance spectroscopy (EIS) measurements were taken in each electrolyte environment before and after the activation process. Before activation, a stable voltage window was determined using CV by expanding the voltage window until the onsets of H_2 and O_2 evolution reactions were reached, as indicated by a sharp increase in current magnitude. After the first series of measurements were finished before activation, the voltage window was adjusted in response to the activation process for carrying out subsequent measurements. CV was performed from scan rates of 2 to 1000 mV s^{-1} , and GCD was tested from 2 to 100 A g^{-1} both before and after activation. EIS was conducted at open circuit potential using a frequency range from 200 kHz to 10 MHz at an amplitude of 10 mV both before and after activation.

4.7. Capacitance Calculations. Gravimetric specific capacitance (F g^{-1}) values were calculated using

$$C_s = \frac{\int_{V_{\text{cathodic}}}^{V_{\text{anodic}}} i \, dV}{m\nu(V_{\text{anodic}} - V_{\text{cathodic}})} \quad (3)$$

where C_s is the gravimetric capacitance, V_{cathodic} (V) and V_{anodic} (V) represent cathodic and anodic potential boundaries, respectively, i (A) represents current, m (g) represents electrode mass, and ν (mV s^{-1}) represents the scan rate.

ASSOCIATED CONTENT

Supporting Information

The Supporting Information is available free of charge at <https://pubs.acs.org/doi/10.1021/acsnano.3c12226>.

Ti_4AlN_3 and $\text{Ti}_4\text{N}_3\text{T}_x$ pore size distributions, SEM images with EDS, full FTIR spectra, CV comparison of pristine and activated $\text{Ti}_4\text{N}_3\text{T}_x$, capacities of pristine and activated $\text{Ti}_4\text{N}_3\text{T}_x$ in H_2SO_4 , MgSO_4 , and KOH , full FTIR spectra of activated $\text{Ti}_4\text{N}_3\text{T}_x$ in each electrolyte, and comparison of reported capacitances and retentions of MXenes (PDF)

AUTHOR INFORMATION

Corresponding Author

Abdoulaye Djire — Artie McFerrin Department of Chemical Engineering and Department of Materials Science & Engineering, Texas A&M University, College Station, Texas 77843, United States; orcid.org/0000-0003-0734-5952; Email: adjire@tamu.edu

Authors

Cheng-Che Hsiao — Artie McFerrin Department of Chemical Engineering, Texas A&M University, College Station, Texas 77843, United States

James Kasten — Artie McFerrin Department of Chemical Engineering, Texas A&M University, College Station, Texas 77843, United States

Denis Johnson — Artie McFerrin Department of Chemical Engineering, Texas A&M University, College Station, Texas 77843, United States

Bright Ngozichukwu — Artie McFerrin Department of Chemical Engineering, Texas A&M University, College Station, Texas 77843, United States

Ray M. S. Yoo — Artie McFerrin Department of Chemical Engineering, Texas A&M University, College Station, Texas 77843, United States

Seungjoo Lee — J. Mike Walker '66 Department of Mechanical Engineering, Texas A&M University, College Station, Texas 77843, United States

Ali Erdemir — J. Mike Walker '66 Department of Mechanical Engineering and Department of Materials Science & Engineering, Texas A&M University, College Station, Texas 77843, United States; orcid.org/0000-0002-6489-9620

Complete contact information is available at:

<https://pubs.acs.org/10.1021/acsnano.3c12226>

Author Contributions

[†]C.-C.H. and J.K. contributed equally to this work.

Notes

The authors declare no competing financial interest.

ACKNOWLEDGMENTS

This work was funded by Texas A&M University (TAMU) and Texas A&M Engineering Experiment Station (TEES). We are grateful to the Department of Chemical Engineering at Texas A&M University and the Governor's University Research Initiative (GURI) for providing funding for the equipment. The authors acknowledge the characterization part of this work was partially performed in the Texas A & M University Materials Characterization Core Facility (RRID: SCR_022202). This research used resources of the Advanced Photon Source, a U.S. Department of Energy (DOE) Office of Science user facility operated for the DOE Office of Science by Argonne National Laboratory under Contract No. DE-AC02-06CH11357. We are also grateful to the Advanced Photon Source (APS) at Argonne National Laboratory (ANL) and to the instrument scientist, Dr. Benjamin Reinhart.

REFERENCES

- (1) Larcher, D.; Tarascon, J. M. Towards greener and more sustainable batteries for electrical energy storage. *Nat. Chem.* **2015**, *7* (1), 19–29.
- (2) Koyampambath, A.; Santillán-Saldivar, J.; McLellan, B.; Sonnemann, G. Supply risk evolution of raw materials for batteries and fossil fuels for selected OECD countries (2000–2018). *Resources Policy* **2022**, *75*, No. 102465.
- (3) Gao, X.; Dong, Y.; Li, S.; Zhou, J.; Wang, L.; Wang, B. MOFs and COFs for Batteries and Supercapacitors. *Electrochemical Energy Reviews* **2020**, *3* (1), 81–126.
- (4) Simon, P.; Gogotsi, Y.; Dunn, B. Where Do Batteries End and Supercapacitors Begin? *Science* **2014**, *343* (6176), 1210–1211.
- (5) Ke, F.-S.; Wu, Y.-S.; Deng, H. Metal-organic frameworks for lithium ion batteries and supercapacitors. *J. Solid State Chem.* **2015**, *223*, 109–121.
- (6) Li, M.; Lu, J.; Chen, Z.; Amine, K. 30 Years of Lithium-Ion Batteries. *Adv. Mater.* **2018**, *30* (33), No. 1800561.
- (7) Wanger, T. C. The Lithium future—resources, recycling, and the environment. *Conservation Letters* **2011**, *4* (3), 202–206.

- (8) Snook, G. A.; Kao, P.; Best, A. S. Conducting-polymer-based supercapacitor devices and electrodes. *J. Power Sources* **2011**, *196* (1), 1–12.
- (9) Meng, Q.; Cai, K.; Chen, Y.; Chen, L. Research progress on conducting polymer based supercapacitor electrode materials. *Nano Energy* **2017**, *36*, 268–285.
- (10) Mastragostino, M.; Arbizzani, C.; Soavi, F. Polymer-based supercapacitors. *J. Power Sources* **2001**, *97–98*, 812–815.
- (11) Zhang, H.; et al. Stable p/n-Dopable Conducting Redox Polymers for High-Voltage Pseudocapacitor Electrode Materials: Structure–Performance Relationship and Detailed Investigation into Charge-Trapping Effect. *Adv. Energy Mater.* **2017**, *7* (21), No. 1701063.
- (12) Theerthagiri, J.; et al. Recent Advances in Metal Chalcogenides (MX; X = S, Se) Nanostructures for Electrochemical Supercapacitor Applications: A Brief Review. *Nanomaterials* **2018**, *8* (4), 256.
- (13) Dahiya, Y.; Hariram, M.; Kumar, M.; Jain, A.; Sarkar, D. Modified transition metal chalcogenides for high performance supercapacitors: Current trends and emerging opportunities. *Coord. Chem. Rev.* **2022**, *451*, No. 214265.
- (14) Shwetha, K. P.; et al. Recent developments of hybrid metal chalcogenides for high performance supercapacitors. *Materials Today: Proceedings* **2023**, *73*, 274–285.
- (15) Yang, P.; et al. Fractal (NixCo1-x)9Se8 Nanodendrite Arrays with Highly Exposed () Surface for Wearable, All-Solid-State Supercapacitor. *Adv. Energy Mater.* **2018**, *8* (26), No. 1801392.
- (16) An, C.; Zhang, Y.; Guo, H.; Wang, Y. Metal oxide-based supercapacitors: progress and prospectives. *Nanoscale Advances* **2019**, *1* (12), 4644–4658.
- (17) Lokhande, C. D.; Dubal, D. P.; Joo, O.-S. Metal oxide thin film based supercapacitors. *Curr. Appl. Phys.* **2011**, *11* (3), 255–270.
- (18) Zhi, M.; Xiang, C.; Li, J.; Li, M.; Wu, N. Nanostructured carbon–metal oxide composite electrodes for supercapacitors: a review. *Nanoscale* **2013**, *5* (1), 72–88.
- (19) Cong, S.; Tian, Y.; Li, Q.; Zhao, Z.; Geng, F. Single-Crystalline Tungsten Oxide Quantum Dots for Fast Pseudocapacitor and Electrochromic Applications. *Adv. Mater.* **2014**, *26* (25), 4260–4267.
- (20) Zhu, Y. G.; Wang, Y.; Shi, Y.; Huang, Z. X.; Fu, L.; Yang, H. Y. Phase Transformation Induced Capacitance Activation for 3D Graphene-CoO Nanorod Pseudocapacitor. *Adv. Energy Mater.* **2014**, *4* (9), No. 1301788.
- (21) Javed, M. S.; et al. High performance solid state flexible supercapacitor based on molybdenum sulfide hierarchical nanospheres. *J. Power Sources* **2015**, *285*, 63–69.
- (22) Das, A.; Raj, B.; Mohapatra, M.; Andersen, S. M.; Basu, S. Performance and future directions of transition metal sulfide-based electrode materials towards supercapacitor/supercapattery. *Wiley Interdisciplinary Reviews: Energy and Environment* **2022**, *11* (1), No. e414.
- (23) Mahmood, Q.; et al. Transition from Diffusion-Controlled Intercalation into Extrinsic Pseudocapacitive Charge Storage of MoS₂ by Nanoscale Heterostructuring. *Adv. Energy Mater.* **2016**, *6* (1), No. 1501115.
- (24) Arulepp, M.; et al. The advanced carbide-derived carbon based supercapacitor. *J. Power Sources* **2006**, *162* (2), 1460–1466.
- (25) Vermisoglou, E. C.; et al. Reduced graphene oxide/iron carbide nanocomposites for magnetic and supercapacitor applications. *J. Alloys Compd.* **2014**, *590*, 102–109.
- (26) Sanger, A.; Kumar, A.; Kumar, A.; Jain, P. K.; Mishra, Y. K.; Chandra, R. Silicon Carbide Nanocauliflowers for Symmetric Supercapacitor Devices. *Ind. Eng. Chem. Res.* **2016**, *55* (35), 9452–9458.
- (27) Tang, J.; et al. Optimizing Ion Pathway in Titanium Carbide MXene for Practical High-Rate Supercapacitor. *Adv. Energy Mater.* **2021**, *11* (4), No. 2003025.
- (28) Ghosh, S.; Jeong, S. M.; Polaki, S. R. A review on metal nitrides/oxy-nitrides as an emerging supercapacitor electrode beyond oxide. *Korean Journal of Chemical Engineering* **2018**, *35* (7), 1389–1408.
- (29) Zhu, C.; et al. All metal nitrides solid-state asymmetric supercapacitors. *Adv. Mater.* **2015**, *27* (31), 4566–4571.
- (30) Djire, A.; Ajenifujah, O. T.; Sleightholme, A. E. S.; Rasmussen, P.; Thompson, L. T. Effects of surface oxygen on charge storage in high surface area early transition-metal carbides and nitrides. *J. Power Sources* **2015**, *275*, 159–166.
- (31) Lu, X.; et al. Improving the Cycling Stability of Metal–Nitride Supercapacitor Electrodes with a Thin Carbon Shell. *Adv. Energy Mater.* **2014**, *4* (4), No. 1300994.
- (32) Conway, B.; Pell, W. Double-layer and pseudocapacitance types of electrochemical capacitors and their applications to the development of hybrid devices. *J. Solid State Electrochem.* **2003**, *7*, 637–644.
- (33) Toupin, M.; Brousse, T.; Bélanger, D. Charge storage mechanism of MnO₂ electrode used in aqueous electrochemical capacitor. *Chem. Mater.* **2004**, *16* (16), 3184–3190.
- (34) Hu, C.-C.; Chen, W.-C. Effects of substrates on the capacitive performance of RuO_x-nH₂O and activated carbon–RuO_x electrodes for supercapacitors. *Electrochim. Acta* **2004**, *49* (21), 3469–3477.
- (35) Choi, D.; Blomgren, G. E.; Kumta, P. N. Fast and Reversible Surface Redox Reaction in Nanocrystalline Vanadium Nitride Supercapacitors. *Adv. Mater.* **2006**, *18* (9), 1178–1182.
- (36) Naguib, M.; et al. Two-Dimensional Nanocrystals Produced by Exfoliation of Ti₃AlC₂. *Adv. Mater.* **2011**, *23* (37), 4248–4253.
- (37) Anasori, B.; Gogotsi, Y. MXenes: trends, growth, and future directions. *Graphene and 2D Materials* **2022**, *7* (3), 75–79.
- (38) Lei, J.-C.; Zhang, X.; Zhou, Z. Recent advances in MXene: Preparation, properties, and applications. *Frontiers of Physics* **2015**, *10* (3), 276–286.
- (39) Johnson, D.; Qiao, Z.; Uwadiunor, E.; Djire, A. Holdups in Nitride MXene’s Development and Limitations in Advancing the Field of MXene. *Small* **2022**, *18* (17), No. 2106129.
- (40) Zhang, N.; Hong, Y.; Yazdanparast, S.; Asle Zaeem, M. Superior structural, elastic and electronic properties of 2D titanium nitride MXenes over carbide MXenes: a comprehensive first principles study. *2D Materials* **2018**, *5* (4), No. 045004.
- (41) Lukatskaya, M. R.; et al. Cation Intercalation and High Volumetric Capacitance of Two-Dimensional Titanium Carbide. *Science* **2013**, *341* (6153), 1502–1505.
- (42) Zhang, T.; Matthews, K.; VahidMohammadi, A.; Han, M.; Gogotsi, Y. Pseudocapacitance of Vanadium Carbide MXenes in Basic and Acidic Aqueous Electrolytes. *ACS Energy Letters* **2022**, *7* (11), 3864–3870.
- (43) Djire, A.; Bos, A.; Liu, J.; Zhang, H.; Miller, E. M.; Neale, N. R. Pseudocapacitive Storage in Nanolayered Ti₂N_{1-x} MXene Using Mg-Ion Electrolyte. *ACS Applied Nano Materials* **2019**, *2* (5), 2785–2795.
- (44) Djire, A.; Zhang, H.; Liu, J.; Miller, E. M.; Neale, N. R. Electrocatalytic and Optoelectronic Characteristics of the Two-Dimensional Titanium Nitride Ti₄N₃T_x MXene. *ACS Appl. Mater. Interfaces* **2019**, *11* (12), 11812–11823.
- (45) Urbankowski, P.; et al. Synthesis of two-dimensional titanium nitride Ti₄N₃ (MXene). *Nanoscale* **2016**, *8* (22), 11385–91.
- (46) Ye, Q.; et al. Exploring the potential of exfoliated ternary ultrathin Ti₄AlN₃ nanosheets for fabricating hybrid patterned polymer brushes. *RSC Adv.* **2015**, *5* (86), 70339–70344.
- (47) Tang, S.; et al. Preparation of Titanium nitride nanomaterials for electrode and application in energy storage. *Results in Physics* **2017**, *7*, 1198–1201.
- (48) Presser, V.; Naguib, M.; Chaput, L.; Togo, A.; Hug, G.; Barsoum, M. W. First-order Raman scattering of the MAX phases: Ti₂AlN, Ti₂AlC_{0.5}N_{0.5}, Ti₂AlC, (Ti_{0.5}V_{0.5})₂AlC, V₂AlC, Ti₃AlC₂, and Ti₃GeC₂. *J. Raman Spectrosc.* **2012**, *43* (1), 168–172.
- (49) Urbankowski, P.; et al. Synthesis of two-dimensional titanium nitride Ti₄N₃ (MXene). *Nanoscale* **2016**, *8* (22), 11385–11391.
- (50) Pranada, E.; Johnson, D.; Yoo, R.; Djire, A. Subsurface oxygen reduction reaction activity on Ti₂N MXene revealed by in situ Raman spectroelectrochemistry. *Sustainable Energy & Fuels* **2023**, *7*, 956.
- (51) Haq, Y.-U.; et al. Synthesis and characterization of 2D MXene: Device fabrication for humidity sensing. *Journal of Science: Advanced Materials and Devices* **2022**, *7* (1), 100390.

- (52) Cao, Y.; et al. Ti–Cl bonds decorated Ti₂N_T x MXene towards high-performance lithium-ion batteries. *2D Materials* **2023**, *10* (1), No. 014001.
- (53) Wang, C.; et al. HCl-Based Hydrothermal Etching Strategy toward Fluoride-Free MXenes. *Adv. Mater.* **2021**, *33* (27), No. 2101015.
- (54) Wang, X.; et al. Surface Redox Pseudocapacitance of Partially Oxidized Titanium Carbide MXene in Water-in-Salt Electrolyte. *ACS Energy Letters* **2022**, *7* (1), 30–35.
- (55) Lützenkirchen-Hecht, D.; Wagemaker, M.; Keil, P.; van Well, A. A.; Frahm, R. Ex situ reflection mode EXAFS at the Ti K-edge of lithium intercalated TiO₂ rutile. *Surf. Sci.* **2003**, *538* (1), 10–22.
- (56) Djire, A.; Bos, A.; Liu, J.; Zhang, H.; Miller, E. M.; Neale, N. R. Pseudocapacitive storage in nanolayered Ti₂N_T x MXene using Mg-ion electrolyte. *ACS Applied Nano Materials* **2019**, *2* (5), 2785–2795.
- (57) Lindström, H.; et al. Li⁺ Ion Insertion in TiO₂ (Anatase). 2. Voltammetry on Nanoporous Films. *J. Phys. Chem. B* **1997**, *101* (39), 7717–7722.
- (58) Ghidui, M.; Lukatskaya, M. R.; Zhao, M.-Q.; Gogotsi, Y.; Barsoum, M. W. Conductive two-dimensional titanium carbide ‘clay’ with high volumetric capacitance. *Nature* **2014**, *516* (7529), 78–81.
- (59) Wang, X.; et al. Two-dimensional V₄C₃MXene as high performance electrode materials for supercapacitors. *Electrochim. Acta* **2019**, *307*, 414–421.
- (60) Halim, J.; et al. Synthesis and Characterization of 2D Molybdenum Carbide (MXene). *Adv. Funct. Mater.* **2016**, *26* (18), 3118–3127.
- (61) Zhao, S.; et al. Flexible Nb₄C₃T_x Film with Large Interlayer Spacing for High-Performance Supercapacitors. *Adv. Funct. Mater.* **2020**, *30* (47), No. 2000815.
- (62) Inman, A.; et al. Shear delamination of multilayer MXenes. *J. Mater. Res.* **2022**, *37* (22), 4006–4016.
- (63) Zhang, J.; Usman, K. A. S.; Judicpa, M. A. N.; Hegh, D.; Lynch, P. A.; Razal, J. M. Applications of X-Ray-Based Characterization in MXene Research. *Small Methods* **2023**, *7*, No. e2201527.
- (64) Qian, A.; Seo, J. Y.; Shi, H.; Lee, J. Y.; Chung, C. H. Surface Functional Groups and Electrochemical Behavior in Dimethyl Sulfoxide-Delaminated Ti₍₃₎ C₍₂₎ T_(x) MXene. *ChemSusChem* **2018**, *11* (21), 3719–3723.
- (65) Hardwick, L. J.; et al. An in situ Raman study of the intercalation of supercapacitor-type electrolyte into microcrystalline graphite. *Electrochim. Acta* **2006**, *52* (2), 675–680.
- (66) Inaba, M.; Yoshida, H.; Ogumi, Z.; Abe, T.; Mizutani, Y.; Asano, M. In Situ Raman Study on Electrochemical Li Intercalation into Graphite. *J. Electrochem. Soc.* **1995**, *142* (1), 20.
- (67) Sole, C.; Drewett, N. E.; Hardwick, L. J. In situ Raman study of lithium-ion intercalation into microcrystalline graphite. *Faraday Discuss.* **2014**, *172* (0), 223–237.
- (68) Djire, A.; Zhang, H.; Reinhart, B. J.; Nwamba, O. C.; Neale, N. R. Mechanisms of Hydrogen Evolution Reaction in Two-Dimensional Nitride MXenes Using In Situ X-Ray Absorption Spectroelectrochemistry. *ACS Catal.* **2021**, *11* (5), 3128–3136.
- (69) Johnson, D.; Hunter, B.; Christie, J.; King, C.; Kelley, E.; Djire, A. Ti₍₂₎N nitride MXene evokes the Mars-van Krevelen mechanism to achieve high selectivity for nitrogen reduction reaction. *Sci. Rep.* **2022**, *12* (1), 657.